The Journal of Chemical Physics

Distinguishing different excitation pathways in two-dimensional terahertz-infrared-visible spectroscopy F

Cite as: J. Chem. Phys. **154**, 174201 (2021); https://doi.org/10.1063/5.0047918
Submitted: 17 February 2021 . Accepted: 12 April 2021 . Published Online: 03 May 2021

Laura Vietze, Ellen H. G. Backus, Mischa Bonn, and Maksim Grechko

COLLECTIONS

Paper published as part of the special topic on Coherent Multidimensional Spectroscopy

F This paper was selected as Featured

ARTICLES YOU MAY BE INTERESTED IN

Two-dimensional terahertz spectroscopy of condensed-phase molecular systems
The Journal of Chemical Physics **154**, 120901 (2021); https://doi.org/10.1063/5.0046664

Direct comparison of amplitude and geometric measures of spectral inhomogeneity using phase-cycled 2D-IR spectroscopy
The Journal of Chemical Physics **154**, 174202 (2021); https://doi.org/10.1063/5.0043961

Progress and challenges in ab initio simulations of quantum nuclei in weakly bonded systems
The Journal of Chemical Physics **154**, 170902 (2021); https://doi.org/10.1063/5.0042572

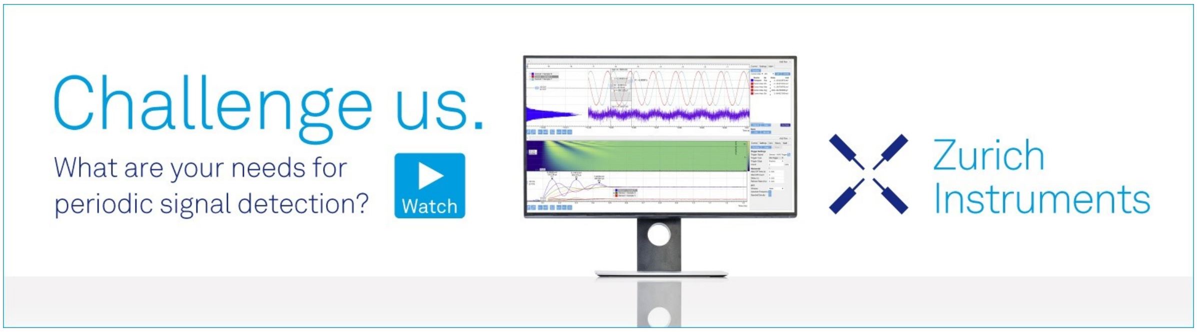

AIP Publishing

The Journal of Chemical Physics ARTICLE scitation.org/journal/jcp

Distinguishing different excitation pathways in two-dimensional terahertz-infrared-visible spectroscopy

Cite as: J. Chem. Phys. 154, 174201 (2021); doi: 10.1063/5.0047918
Submitted: 17 February 2021 • Accepted: 12 April 2021 •
Published Online: 3 May 2021

Laura Vietze,[1] **Ellen H. G. Backus,**[1,2] **Mischa Bonn,**[1] **and Maksim Grechko**[1,a)]

AFFILIATIONS

[1] Department of Molecular Spectroscopy, Max Planck Institute for Polymer Research, Ackermannweg 10, D-55128 Mainz, Germany
[2] Department of Physical Chemistry, University of Vienna, Währinger Strasse 42, 1090 Vienna, Austria

Note: This paper is part of the JCP Special Topic on Coherent Multidimensional Spectroscopy.
[a)] **Author to whom correspondence should be addressed:** grechko@mpip-mainz.mpg.de

ABSTRACT

In condensed molecular matter, low-frequency modes (LFMs) associated with specific molecular motions are excited at room temperature and determine essential physical and chemical properties of materials. LFMs, with typical mode energies of up to ~500 cm^{-1} (62 meV), contribute significantly to thermodynamic parameters and functions (e.g., heat capacity and entropy) and constitute the basis for room temperature molecular dynamics (e.g., conformational fluctuations and change). LFMs are often analyzed indirectly by the measurement of their effect on specific high-frequency modes (HFMs); the LFM–HFM coupling is reflected in the lineshape, as well as in the spectral and angular diffusion of the HFM. Two-dimensional terahertz-infrared-visible (2D TIRV) spectroscopy allows measuring the LFM–HFM coupling directly and can thereby provide new insights into the strength and nature of the coupling and the character of LFMs. However, the interference between the different signals generated by different excitation pathways can complicate 2D TIRV spectra, preventing a straightforward analysis. Here, we develop an experimental method to distinguish different excitation pathways in 2D TIRV spectroscopy and plot them separately in different quadrants of a 2D spectrum. We validate this method by measuring the spectra of CaF_2 and nitrogen gas. For CaF_2, only sum-frequency mixing between infrared and terahertz fields generates the signal. In contrast, for N_2, only difference-frequency mixing is observed. We then use this method to separate sum- and difference-frequency pathways in the 2D TIRV spectrum of liquid water, verifying the previous interpretation of the lineshape of the 2D TIRV spectrum of water.

INTRODUCTION

Infrared vibrational spectroscopy is often used to study ultrafast dynamics on a nanometer length scale in condensed phase substances. For example, homogeneous line broadening and spectral diffusion of a vibrational chromophore reflect the rates of local structure fluctuations and are measured in linear infrared absorption spectroscopy and non-linear two-dimensional infrared (2D IR) spectroscopy.[1–3] Another example is the decay of vibrational excitation anisotropy, which is measured in transient absorption spectroscopy. In the absence of intermolecular energy transfer, the anisotropy decay is caused by the reorientation of a vibrational chromophore due to intra- and/or inter-molecular motions and, thus, reflects the rate of molecular rotation in the densely packed environment of the condensed phase.[4,5] The typical time scale of molecular reorientation and molecular structure fluctuations measured by vibrational spectroscopy is in the range of a few tens of femtoseconds to several picoseconds. The energies of such motions are in the terahertz frequency range (<500 cm^{-1}), and they constitute low-frequency modes (LFMs) of a sample. Generally speaking, the capability of infrared vibrational spectroscopy to reveal the molecular dynamics results from the coupling between a high-frequency vibrational chromophore (O—H, N—H, C=O, C=N stretch, etc.) and low-frequency intra- and inter-molecular motions. Thus, infrared vibrational spectroscopy employs a high-frequency mode (HFM) and measures its coupling with the low-frequency modes (LFMs) of molecular motions to reveal the latter. The measurement of the HFM–LFM coupling, in this case, is implemented indirectly, i.e., by probing the state of the HFM only. To measure the coupling directly, we have recently developed two-dimensional Terahertz-InfraRed-Visible (2D TIRV) spectroscopy.[6,7] In 2D TIRV spectroscopy, we excite LFMs and HFMs using broadband terahertz (THz) and mid-infrared (IR) pulses, respectively. Coupled LFM and HFM resonances enhance the mixing of the THz and IR fields, which is then reflected in the signal emitted by a sample. We have previously used 2D TIRV spectroscopy to measure the coupling in liquid water and organic–inorganic perovskites.[6,7] However, in these previous implementations of 2D TIRV spectroscopy, we could not separate distinct excitation pathways. The superposition of different excitation pathways complicates the spectra significantly. To facilitate the analysis of experimental data, signals generated by different excitation pathways need to be separated. In this work, we develop a procedure to separate these different signals and plot them individually in the two-dimensional spectrum.

Signal generation by different excitation pathways is common in all spectroscopy techniques. In 2D techniques, the different excitation pathways are usually classified as rephasing and non-rephasing, depending on whether the oscillation frequencies of the two coherent evolution periods have the same (non-rephasing) or opposite (rephasing) sign. Sometimes, the superposition of different signals can be beneficial in spectroscopy. A prominent example is absorption spectroscopy, where the superposition of signals from two complex conjugate pathways produces an absorption spectrum rather than a dispersion or mixed absorption–dispersion spectrum. A similar advantage—obtaining an absorptive spectrum—is achieved in 2D IR, 2D THz, and 2D electronic spectroscopy by summing signals from the rephasing and non-rephasing excitation pathways.[1,8–10] In contrast, in 2D TIRV spectroscopy (similar to 2D Raman-THz spectroscopy[11–13] and 2D THz-THz-Raman spectroscopy[14–16]), the rephasing and non-rephasing excitation pathways are not symmetric. Non-rephasing and rephasing excitations can be associated with sum and difference frequency mixing of the IR and THz electromagnetic fields, respectively (such as mixing of infrared fields in other spectroscopy techniques[17–22]). Their superposition does not produce an absorptive spectrum that is intuitive to interpret. Instead, the superposition of non-rephasing and rephasing excitation pathways in 2D TIRV spectroscopy generates an interference pattern, as illustrated by the 2D TIRV spectrum of liquid water in Fig. 1. It shows a complicated pattern and a minimum intensity at $\Omega_2 \approx 3250\ \mathrm{cm}^{-1}$ due to the interference of different excitation pathways, as proposed in Ref. 6.

Consequently, to simplify the spectrum, we need to separate rephasing and non-rephasing excitation pathways, which are all excited in 2D TIRV spectroscopy.[6,23] In some 2D spectroscopy techniques, such as triple sum-frequency mixing, infrared-infrared-visible, and 2D DOVE,[17–21,24] the sum and difference frequency mixing signals are emitted at unique frequencies and can be readily distinguished. The unique frequencies of the signals are due to the bandwidth of the laser pulses being much narrower than their carrier frequencies. In our case, the bandwidth of the IR pulse employed in the experiment ($\approx 350\ \mathrm{cm}^{-1}$) is comparable with the frequency range of the THz pulse. Thus, only the signal frequency is not sufficient to assign it to sum and difference frequency mixing processes. To separate these different excitation pathways, we need to determine the sign of the frequency of both the THz and IR fields producing the signal. The THz frequency, together with its sign, was already resolved in our previous work by performing Fourier transformation of the measured time-domain data. The sign of the frequency of the IR field was not previously resolved. Here, we complete the separation of the excitation pathways. To this end, we adopt the approach of phase-resolved SFG spectroscopy, where the separation of positive and negative IR frequencies is carried out by offsetting the local oscillator (LO) over time relative to the signal.[25,26]

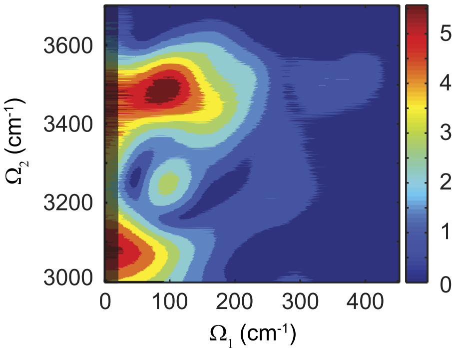

FIG. 1. Absolute-value 2D TIRV spectrum of H_2O.[6] Note the different local maxima in the signal, which are shown to originate from the interference of distinct excitation pathways.

In the theoretical section below, we consider the principles of 2D TIRV spectroscopy and formulate a procedure to separate the signals from the different rephasing and non-rephasing excitation pathways. We validate this procedure using CaF_2 and nitrogen gas as two model samples. After validating the approach, we use it to obtain various components of the 2D TIRV response of liquid water, thereby verifying the previous interpretation of the 2D TIRV spectrum of liquid water.

PRINCIPLES OF 2D TIRV SPECTROSCOPY

Here, we provide a brief and simplified description of the principles of 2D TIRV spectroscopy. The supplementary material and Refs. 6 and 23 contain additional information. 2D TIRV spectroscopy employs broadband terahertz (THz), broadband mid-infrared (IR), and narrowband visible (VIS) pulses to excite a sample. These interactions generate a signal that is spectrally resolved and detected in the $\Omega_{\mathrm{sig}} = \Omega_{\mathrm{VIS}} + \Omega_{\mathrm{IR}} \pm \Omega_{\mathrm{THz}}$ frequency range. In general, interactions of the sample with THz and IR pulses can be resonant as well as non-resonant. Resonant interactions enhance the 2D TIRV signal and can occur via different excitation pathways. To illustrate this, we consider a simple five-level system shown in Fig. 2 as an example. The system is composed of two sub-systems

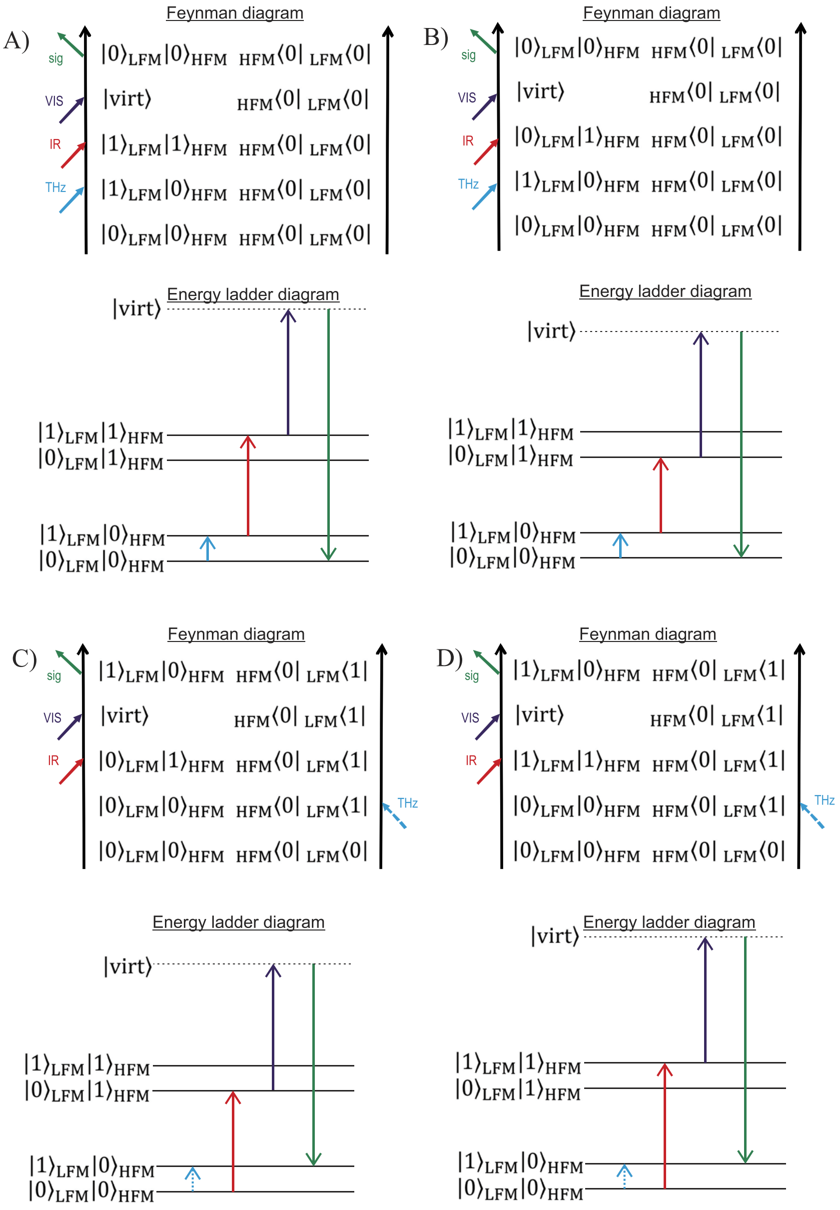

FIG. 2. Excitation pathways for 2D TIRV spectroscopy. Each excitation pathway is shown using both Feynman and energy ladder diagrams. Pathways A/B and C/D are non-rephasing and rephasing, respectively.

corresponding to high- and low-frequency oscillators. The high-frequency oscillator is represented by its ground and excited vibrational states $|0\rangle_{HFM}$ and $|1\rangle_{HFM}$, respectively. Similarly, the states $|0\rangle_{LFM}$ and $|1\rangle_{LFM}$ represent those of the low-frequency oscillator. Hence, the states of the complete system are $|i\rangle_{LFM}|j\rangle_{HFM}$ $(i, j = 0, 1)$. In addition to the vibrational states, the system has a virtual state $|virt\rangle$, which represents the non-resonant electron excitation (polarizability). When such a system interacts successively with the THz, IR, and VIS pulses, the excitation pathways are represented by four distinct Feynman/energy ladder diagrams, as shown in Fig. 2 (there are other four complex conjugate pathways, which contain the same information about the system).[1,27,28] The THz pulse excites a transition between the ground and excited states of the low-frequency oscillator. After THz excitation, the IR pulse promotes a transition to the vibrationally excited state of the high-frequency oscillator. The IR transition can conserve the state of the LFM (diagrams A and C) or change it (diagrams B and D). To keep the discussion simple, we do not consider another sequence where the first interaction is with the IR pulse. A more general description, including all possible interaction sequences, is given in the supplementary material.

A general view of a 2D TIRV spectrum is shown in Fig. 3. The signal is plotted as a function of the THz excitation frequency ω_1 and the combined THz and IR excitation frequency ω_2. The latter,

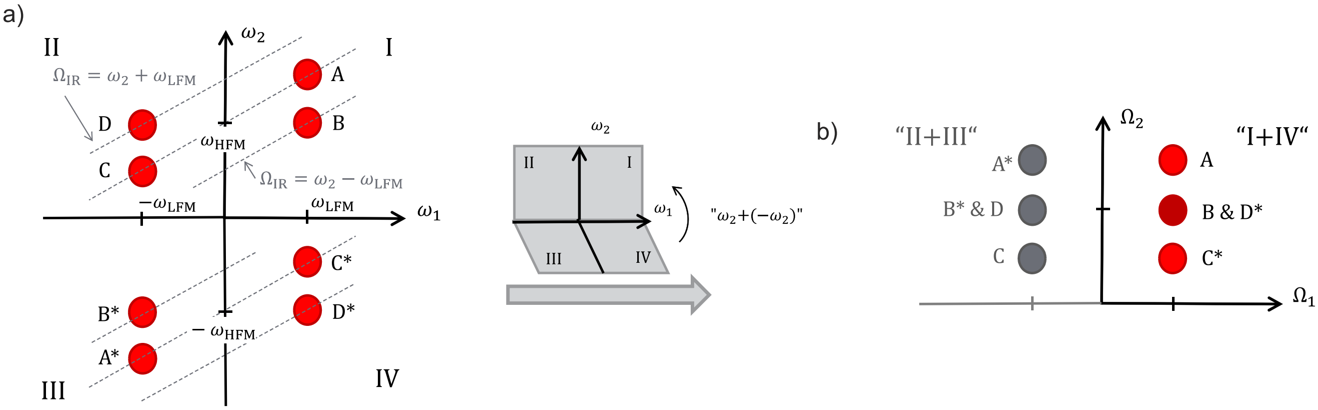

FIG. 3. Schematic of the 2D TIRV spectrum: (a) signals generated by excitation pathways A–D shown in Fig. 2 and their complex conjugate pathways A*–D* are shown in four quadrants of a 2D TIRV spectrum; the dashed lines show points in the spectrum, for which the signal is generated by the same IR frequency, (b) the 2D TIRV spectrum, which results from the superposition of quadrants I and IV, as illustrated by the gray cartoon between panels (a) and (b). In (b), the superposition of quadrants II and III is shown in gray.

ω_2, is the frequency of a coherent state that is excited in a sample after the interaction with both THz and IR pulses. The excitation pathways shown in Fig. 2 appear in the 2D TIRV spectrum at different positions. The signals generated by the pathways A–D and their complex conjugates A*–D* are shown schematically in Fig. 3(a). The signal generated via the non-rephasing pathways A and B oscillates at positive frequencies ω_1 and ω_2 after THz and IR excitations, respectively. This signal appears in the first, upper right quadrant of the spectrum. In contrast, the signals generated via the rephasing pathways C and D oscillate at negative frequency ω_1 and positive frequency ω_2 and appear in the second quadrant of the spectrum. Another distinction is the location of the signals A and B in the first quadrant. Whereas both of these signals have the same frequency ω_1, their ω_2-frequencies are different. The frequency ω_2 of pathway B equals the frequency of the HFM vibration. The frequency ω_2 of pathway A equals the sum of the frequencies of the HFM and the LFM. Thus, the resonant signal A appears offset to a higher frequency relative to the frequency of the HFM. In the second quadrant, signal D is located at the frequency ω_1 of the LFM and the frequency ω_2 of the HFM, whereas the signal generated via pathway C has a ω_2-frequency equal to the difference in the HFM and LFM frequencies. In general, the resonant 2D TIRV signal has a ω_2-frequency of the HFM when the two-quantum transition (transition when the excitation of both LFM and HFM changes) happens during interaction with the IR pulse. As shown in Fig. 3(a), the complex conjugate pathways A*, B*, C*, and D* oscillate with the same ω_1- and ω_2-frequencies as the pathways A–D, with, however, an opposite sign. Accordingly, signals generated via pathways A*/B* and C*/D* appear in the third and fourth quadrants, respectively.

We note that the ω_2-frequency of the 2D TIRV signal never equals the IR frequency (Ω_{IR}) that promotes the transition of the HFM. This is due to the 2D TIRV excitation taking place only via coherence states, and being in contrast to, e.g., 2D IR spectroscopy, which employs a population state as well. For instance, for pathway A shown in Fig. 2, the IR frequency is equal to that of the HFM, and the signal appears at a higher ω_2 frequency. Signal B appears at the frequency of the HFM, but it is generated by IR light with a frequency lower than the HFM frequency. Depending on the excitation pathway, the IR frequency can be also higher than ω_{HFM}, which is the case for pathway D. Therefore, in 2D TIRV spectroscopy, a resonant peak can have ω_2-frequency of the HFM but never the frequency of the IR light that generates the signal (Table I). However, for small ω_1, the difference between the IR frequency and ω_2 is small.

With the experimental approach of our previous work, we could not separate all four quadrants of a 2D TIRV spectrum. This limitation stems from how the ordinate axis of the 2D spectrum is derived. In our previous experiments, this frequency is obtained by subtracting the frequency of the VIS pulse from the frequency of the signal, $\Omega_2 = \Omega_{sig} - \Omega_{VIS}$. Hence, Ω_2 cannot be negative, and we distinguish it from ω_2 in Fig. 3(a), which can be both positive and negative. In our previous work, we analyzed the superposition of the first and fourth quadrants of the spectrum,[6,7] as is shown schematically in Fig. 3(b). However, these quadrants contain physically distinct information: non-rephasing response in the first quadrant probed by sum frequency mixing and rephasing response in the fourth quadrant probed by difference frequency mixing. In the present work, we elaborate a quadrant separation (QS) procedure, which enables derivation of the ω_2-frequency and

TABLE I. Frequencies ω_1, ω_2, and Ω_{IR} for different excitation pathways in 2D TIRV spectroscopy.

Pathway	A	B	C	D
ω_1	ω_{LFM}	ω_{LFM}	$-\omega_{LFM}$	$-\omega_{LFM}$
ω_2	$\omega_{HFM} + \omega_{LFM}$	ω_{HFM}	$\omega_{HFM} - \omega_{LFM}$	ω_{HFM}
Ω_{IR}	ω_{HFM}	$\omega_{HFM} - \omega_{LFM}$	ω_{HFM}	$\omega_{HFM} + \omega_{LFM}$

partitions the total 2D TIRV signal into sum and difference frequency generation components (between the IR and THz fields). For the resonant signal, this partitioning isolates different excitation pathways in different quadrants of the spectrum [Fig. 3(a)], which facilitates their analysis.

THEORETICAL DESCRIPTION OF THE QUADRANT SEPARATION PROCEDURE IN 2D TIRV SPECTROSCOPY

To illustrate our approach to the quadrant separation in 2D TIRV spectroscopy, we consider a spectrum as it is measured in optical spectroscopy using a spectrometer and heterodyne detection. A spectrum at a detector is given by the interference of the signal (E_{sig}) and the local oscillator fields (E_{LO}) and can be written as

$$I_{\mathrm{det}}(\omega_{\mathrm{sig}}) = E_{\mathrm{sig}}(\omega_{\mathrm{sig}})E^{*}_{\mathrm{LO}}(\omega_{\mathrm{sig}}) + E^{*}_{\mathrm{sig}}(\omega_{\mathrm{sig}})E_{\mathrm{LO}}(\omega_{\mathrm{sig}}). \tag{1}$$

Because $E^{*}_{\mathrm{sig}}(\omega_{\mathrm{sig}}) = E_{\mathrm{sig}}(-\omega_{\mathrm{sig}})$, the measured spectrum contains a signal at both positive and negative frequencies. If we now delay over time the local oscillator by Δ relative to the signal, the spectrum becomes

$$\begin{aligned} I_{\mathrm{det}}(\omega_{\mathrm{sig}}) &= E_{\mathrm{sig}}(\omega_{\mathrm{sig}})E_{\mathrm{LO}}(-\omega_{\mathrm{sig}})e^{i\omega_{\mathrm{sig}}\Delta} \\ &\quad + E_{\mathrm{sig}}(-\omega_{\mathrm{sig}})E_{\mathrm{LO}}(\omega_{\mathrm{sig}})e^{-i\omega_{\mathrm{sig}}\Delta}. \end{aligned} \tag{2}$$

The first (second) term in this equation can be considered as oscillating with a periodicity of $1/\Delta$ ($-1/\Delta$) along the axis of ω_{sig} due to the exponential factor. Thus, after Fourier transformation of I_{det} along the ω_{sig}-axis, the $E_{\mathrm{sig}}(\omega_{\mathrm{sig}})$- and $E_{\mathrm{sig}}(-\omega_{\mathrm{sig}})$-containing signals appear at Δ and $-\Delta$ in the conjugate space, respectively. This allows us to separate them and analyze them individually. This approach is widely used in phase-resolved SFG spectroscopy,[25,26,29–32] and below, we rigorously derive the corresponding equations for 2D TIRV spectroscopy.

In 2D TIRV spectroscopy, we measure the spectrum by four-wave mixing of a broadband terahertz (THz), a broadband mid-infrared (IR), and a narrowband visible (VIS) pulse in the sample. We use heterodyne detection and measure the interference of the signal and local oscillator (LO) pulses at the detector. After processing the data, the 2D TIRV spectrum Γ is given by [Eq. (S16), supplementary material]

$$\begin{aligned} \Gamma(\Omega_2 + \Omega_{\mathrm{VIS}}, \Omega_1) \propto &\left\{S^{(3)}(\Omega_2 + \Omega_{\mathrm{VIS}}, \Omega_2, \Omega_1) + S^{(3)}(\Omega_2 + \Omega_{\mathrm{VIS}}, \Omega_2, \Omega_2 - \Omega_1)\right\} \\ &\times E_{\mathrm{THz}}(\Omega_1)E_{\mathrm{IR}}(\Omega_2 - \Omega_1)E^{0}_{\mathrm{VIS}}E_{\mathrm{LO}}(-\Omega_2 - \Omega_{\mathrm{VIS}}) \\ &+ \left\{S^{(3)}(-\Omega_2 - \Omega_{\mathrm{VIS}}, -\Omega_2, \Omega_1) + S^{(3)}(-\Omega_2 - \Omega_{\mathrm{VIS}}, -\Omega_2, -\Omega_2 - \Omega_1)\right\} \\ &\times E_{\mathrm{THz}}(\Omega_1)E_{\mathrm{IR}}(-\Omega_2 - \Omega_1)E^{0}_{\mathrm{VIS}}{}^{*}E_{\mathrm{LO}}(\Omega_2 + \Omega_{\mathrm{VIS}}), \end{aligned} \tag{3}$$

where $E_{\mathrm{THz}}(\omega)$, $E_{\mathrm{IR}}(\omega)$, and $E_{\mathrm{LO}}(\omega)$ are the electromagnetic fields of the THz, IR, and LO pulses, respectively. The VIS pulse is approximated by an infinitely narrow spectrum, with the frequency $\Omega_{\mathrm{VIS}} > 0$ and amplitude $|E^{0}_{\mathrm{VIS}}|$. $S^{(3)}(\omega_3, \omega_2, \omega_1)$ is the spectrum of the third-order non-linear optical response function of the sample. The coordinate Ω_1 of the two-dimensional spectrum Γ reflects the LFM coherence excited by the THz pulse. The coordinate Ω_2 represents the frequency of the coherence state after interaction with the THz and IR pulses (Fig. 2).

In Eq. (1), we use capital Ω to denote frequencies and distinguish these variables from the small ω in the previous section for the following reason. It is important that the frequencies Ω_1 and Ω_2 are derived in different ways in the experiment. The coordinate Ω_1 is obtained by Fourier transformation of the acquired data along the varied time delay of the THz pulse relative to the IR/VIS pulse pair. It can be positive as well as negative ($-\infty < \Omega_1 < +\infty$). Thus, the response function $S^{(3)}(\ldots, \ldots, \Omega_1 > 0)$ and $S^{(3)}(\ldots, \ldots, \Omega_1 < 0)$ appears in the different quadrants $\Gamma(\ldots, \Omega_1 > 0)$ and $\Gamma(\ldots, \Omega_1 < 0)$ of the 2D TIRV spectrum, respectively. In contrast, the coordinate Ω_2 is obtained from the frequency of the detected signal by subtracting Ω_{VIS}. The frequency of the signal is measured using a grating-based spectrometer and is positive-valued. Thus, the coordinate Ω_2 is positive ($\Omega_2 > 0$), as shown in Eq. (3). The inability of the grating-based spectrometer to separate positive and negative frequencies causes the superposition of the two parts of the response function, $S^{(3)}_{+} = S^{(3)}(\ldots, \Omega_2, \ldots)$ and $S^{(3)}_{-} = S^{(3)}(\ldots, -\Omega_2, \ldots)$, in the 2D TIRV spectrum [schematically shown in Fig. 3(b)]. These two parts, similar to the rephasing and non-rephasing spectra in 2D IR spectroscopy, have different physical meanings and need to be separated.

To separate $S^{(3)}_{+}$ and $S^{(3)}_{-}$, we adopt the method developed for phase-resolved SFG spectroscopy.[25] Phase-resolved SFG spectroscopy makes use of an increased time delay between the LO and signal pulses at the detector. A selective Fourier transformation of the interference between the LO and signal allows separating the $\chi^{(2)}$ and $\chi^{(2)^{*}}$ parts of the spectrum. Below, we show that by using a similar procedure in or for 2D TIRV spectroscopy, we can separate the different parts, $S^{(3)}_{+}$ and $S^{(3)}_{-}$, of the measured response function.

When the LO pulse, $E_{\mathrm{LO}}(t)$ is shifted by Δ over time, its spectrum is modulated by a linear phase shift. In our notations, the electric field of the shifted pulse $E'_{\mathrm{LO}}(t) = E_{\mathrm{LO}}(t + \Delta)$ and $\Delta > 0$ corresponds to an LO pulse that arrives at the detector at an earlier time. The 2D TIRV spectrum measured with the offset LO pulse is given by

$$\begin{aligned}\Gamma(\Omega_2+\Omega_{\mathrm{VIS}},\Omega_1) \propto{}& \left\{S^{(3)}(\Omega_2+\Omega_{\mathrm{VIS}},\Omega_2,\Omega_1)+S^{(3)}(\Omega_2+\Omega_{\mathrm{VIS}},\Omega_2,\Omega_2-\Omega_1)\right\}\\ &\times E_{\mathrm{THz}}(\Omega_1)E_{\mathrm{IR}}(\Omega_2-\Omega_1)E^0_{\mathrm{VIS}}E_{\mathrm{LO}}(-\Omega_2-\Omega_{\mathrm{VIS}})e^{i(\Omega_2+\Omega_{\mathrm{VIS}})\Delta}\\ &+\left\{S^{(3)}(-\Omega_2-\Omega_{\mathrm{VIS}},-\Omega_2,\Omega_1)+S^{(3)}(-\Omega_2-\Omega_{\mathrm{VIS}},-\Omega_2,-\Omega_2-\Omega_1)\right\}\\ &\times E_{\mathrm{THz}}(\Omega_1)E_{\mathrm{IR}}(-\Omega_2-\Omega_1)E^{0}_{\mathrm{VIS}}{}^{*}E_{\mathrm{LO}}(\Omega_2+\Omega_{\mathrm{VIS}})e^{-i(\Omega_2+\Omega_{\mathrm{VIS}})\Delta}.\end{aligned}\tag{4}$$

To separate the $S^{(3)}_{+}$ and $S^{(3)}_{-}$ parts of the response function, we perform Fourier transformation of the spectrum Γ along the spectrometer frequency $\Omega_2+\Omega_{\mathrm{VIS}}$,

$$\begin{aligned}\Gamma(x,\Omega_1) \propto{}& \int_{-\infty}^{+\infty} d(\Omega_2+\Omega_{\mathrm{VIS}})\left\{S^{(3)}(\Omega_2+\Omega_{\mathrm{VIS}},\Omega_2,\Omega_1)+S^{(3)}(\Omega_2+\Omega_{\mathrm{VIS}},\Omega_2,\Omega_2-\Omega_1)\right\}\\ &\times E_{\mathrm{THz}}(\Omega_1)E_{\mathrm{IR}}(\Omega_2-\Omega_1)E^0_{\mathrm{VIS}}E_{\mathrm{LO}}(-\Omega_2-\Omega_{\mathrm{VIS}})e^{i(\Omega_2+\Omega_{\mathrm{VIS}})\Delta}e^{-i(\Omega_2+\Omega_{\mathrm{VIS}})x}\\ &+\int_{-\infty}^{+\infty} d(\Omega_2+\Omega_{\mathrm{VIS}})\left\{S^{(3)}(-\Omega_2-\Omega_{\mathrm{VIS}},-\Omega_2,\Omega_1)+S^{(3)}(-\Omega_2-\Omega_{\mathrm{VIS}},-\Omega_2,-\Omega_2-\Omega_1)\right\}\\ &\times E_{\mathrm{THz}}(\Omega_1)E_{\mathrm{IR}}(-\Omega_2-\Omega_1)E^{0}_{\mathrm{VIS}}{}^{*}E_{\mathrm{LO}}(\Omega_2+\Omega_{\mathrm{VIS}})e^{-i(\Omega_2+\Omega_{\mathrm{VIS}})\Delta}e^{-i(\Omega_2+\Omega_{\mathrm{VIS}})x}.\end{aligned}\tag{5}$$

In phase-resolved SFG spectroscopy, a similar transformation is often considered as the transformation of the signal from the frequency (spectrum) back to the time domain (pulse).[25] We can write the hybrid time-frequency function $\Gamma(x, \Omega_1)$ as two terms A' (for Ω_2) and A'' (for $-\Omega_2$),

$$\Gamma(x,\Omega_1) = A'(x-\Delta,\Omega_1) + A''(x+\Delta,\Omega_1).\tag{6}$$

Here, $A'(x, \Omega_1)$ is given by

$$\begin{aligned}A'(x,\Omega_1) \propto{}& \int_{-\infty}^{+\infty} d(\Omega_2+\Omega_{\mathrm{VIS}})\left\{S^{(3)}(\Omega_2+\Omega_{\mathrm{VIS}},\Omega_2,\Omega_1)+S^{(3)}(\Omega_2+\Omega_{\mathrm{VIS}},\Omega_2,\Omega_2-\Omega_1)\right\}\\ &\times E_{\mathrm{THz}}(\Omega_1)E_{\mathrm{IR}}(\Omega_2-\Omega_1)E^0_{\mathrm{VIS}}E_{\mathrm{LO}}(-\Omega_2-\Omega_{\mathrm{VIS}})e^{-i(\Omega_2+\Omega_{\mathrm{VIS}})x},\end{aligned}\tag{7}$$

and $A''(x, \Omega_1)$ is given by

$$\begin{aligned}A''(x,\Omega_1) \propto{}& \int_{-\infty}^{+\infty} d(\Omega_2+\Omega_{\mathrm{VIS}})\left\{S^{(3)}(-\Omega_2-\Omega_{\mathrm{VIS}},-\Omega_2,\Omega_1)+S^{(3)}(-\Omega_2-\Omega_{\mathrm{VIS}},-\Omega_2,-\Omega_2-\Omega_1)\right\}\\ &\times E_{\mathrm{THz}}(\Omega_1)E_{\mathrm{IR}}(-\Omega_2-\Omega_1)E^{0}_{\mathrm{VIS}}{}^{*}E_{\mathrm{LO}}(\Omega_2+\Omega_{\mathrm{VIS}})e^{-i(\Omega_2+\Omega_{\mathrm{VIS}})x}.\end{aligned}\tag{8}$$

In principle, the response functions $S^{(3)}_{+}$ and $S^{(3)}_{-}$ can be obtained by the inverse Fourier transformation of $A'(x, \Omega_1)$ and $A''(x, \Omega_1)$, respectively. For any physical response function $S^{(3)}$ and electromagnetic fields E_{THz}, E_{IR}, and E_{LO}, the functions $A'(x, \Omega_1)$ and $A''(x, \Omega_1)$ are non-zero only for a specific range of $x = [-a, +a]$, as schematically shown in Fig. 4(a). It is also likely that these functions overlap within the range $x = [-a, +a]$ and thus cannot be separated. However, in the time-frequency function $\Gamma(x, \Omega_1)$, the time delay Δ of the LO pulse shifts A' and A'' in opposite directions along the coordinate axis x [Eq. (6), Fig. 4(b)]. In principle, for any physical $A'(x, \Omega_1)$ and $A''(x, \Omega_1)$, we can find a value of the time delay Δ that will separate them. For this Δ, the range $x = [-a + \Delta, +a + \Delta]$, where $A'(x - \Delta, \Omega_1)$ is non-zero, and the range $x = [-a - \Delta, +a - \Delta]$, where $A''(x + \Delta, \Omega_1)$ is non-zero, do not overlap.

When $A'(x - \Delta, \Omega_1)$ and $A''(x + \Delta, \Omega_1)$ are separated, we can perform their inverse Fourier transformation over the coordinate x

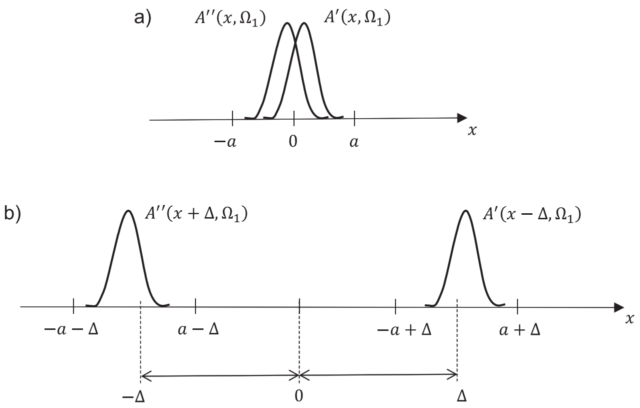

FIG. 4. Schematic visualization of functions $A'(x, \Omega_1)$ and $A''(x, \Omega_1)$ as a function of variable x [panel (a)] and their position along the coordinate axis x after introducing a time delay Δ [panel (b)].

separately and obtain the spectra $\Gamma'(\omega, \Omega_1)$ and $\Gamma''(\omega, \Omega_1)$,

$$\begin{aligned}\Gamma'(\omega,\Omega_1) &= \int_{-a+\Delta}^{+a+\Delta} A'(x-\Delta,\Omega_1)e^{i\omega x}dx\\ &= \int_{-\infty}^{+\infty} A'(x-\Delta,\Omega_1)e^{i\omega x}dx,\end{aligned} \tag{9}$$

$$\begin{aligned}\Gamma''(\omega,\Omega_1) &= \int_{-a-\Delta}^{+a-\Delta} A''(x+\Delta,\Omega_1)e^{i\omega x}dx\\ &= \int_{-\infty}^{+\infty} A''(x+\Delta,\Omega_1)e^{i\omega x}dx.\end{aligned} \tag{10}$$

By substituting Eq. (7) into Eq. (9), we obtain

$$\begin{aligned}\Gamma'(\omega,\Omega_1) \propto{}& \int_{-\infty}^{+\infty}\int_{-\infty}^{+\infty} d(\Omega_2+\Omega_{\mathrm{VIS}})dx\Big\{S^{(3)}(\Omega_2+\Omega_{\mathrm{VIS}},\Omega_2,\Omega_1)+S^{(3)}(\Omega_2+\Omega_{\mathrm{VIS}},\Omega_2,\Omega_2-\Omega_1)\Big\}\\ &\times E_{\mathrm{THz}}(\Omega_1)E_{\mathrm{IR}}(\Omega_2-\Omega_1)E^{0}_{\mathrm{VIS}}E_{\mathrm{LO}}(-\Omega_2-\Omega_{\mathrm{VIS}})e^{-i(\Omega_2+\Omega_{\mathrm{VIS}})(x-\Delta)}e^{i\omega x}\\ ={}& \int_{-\infty}^{+\infty} d(\Omega_2+\Omega_{\mathrm{VIS}})\Big\{S^{(3)}(\Omega_2+\Omega_{\mathrm{VIS}},\Omega_2,\Omega_1)+S^{(3)}(\Omega_2+\Omega_{\mathrm{VIS}},\Omega_2,\Omega_2-\Omega_1)\Big\}\\ &\times E_{\mathrm{THz}}(\Omega_1)E_{\mathrm{IR}}(\Omega_2-\Omega_1)E^{0}_{\mathrm{VIS}}E_{\mathrm{LO}}(-\Omega_2-\Omega_{\mathrm{VIS}})e^{i(\Omega_2+\Omega_{\mathrm{VIS}})\Delta}\int_{-\infty}^{-\infty} e^{-i(\Omega_2+\Omega_{\mathrm{VIS}})x}e^{i\omega x}dx\\ ={}& \int_{-\infty}^{+\infty} d(\Omega_2+\Omega_{\mathrm{VIS}})\Big\{S^{(3)}(\Omega_2+\Omega_{\mathrm{VIS}},\Omega_2,\Omega_1)+S^{(3)}(\Omega_2+\Omega_{\mathrm{VIS}},\Omega_2,\Omega_2-\Omega_1)\Big\}\\ &\times E_{\mathrm{THz}}(\Omega_1)E_{\mathrm{IR}}(\Omega_2-\Omega_1)E^{0}_{\mathrm{VIS}}E_{\mathrm{LO}}(-\Omega_2-\Omega_{\mathrm{VIS}})e^{i(\Omega_2+\Omega_{\mathrm{VIS}})\Delta}\delta(\omega-\Omega_2-\Omega_{\mathrm{VIS}})\\ ={}& \Big\{S^{(3)}(\Omega_2+\Omega_{\mathrm{VIS}},\Omega_2,\Omega_1)+S^{(3)}(\Omega_2+\Omega_{\mathrm{VIS}},\Omega_2,\Omega_2-\Omega_1)\Big\}\\ &\times E_{\mathrm{THz}}(\Omega_1)E_{\mathrm{IR}}(\Omega_2-\Omega_1)E^{0}_{\mathrm{VIS}}E_{\mathrm{LO}}(-\Omega_2-\Omega_{\mathrm{VIS}})e^{i(\Omega_2+\Omega_{\mathrm{VIS}})\Delta}\big|_{\Omega_2+\Omega_{\mathrm{VIS}}=\omega}.\end{aligned} \tag{11}$$

Equation (9) can be written as

$$\begin{aligned}\Gamma'(\Omega_2+\Omega_{\mathrm{VIS}},\Omega_1) \propto{}& \Big\{S^{(3)}(\Omega_2+\Omega_{\mathrm{VIS}},\Omega_2,\Omega_1)+S^{(3)}(\Omega_2+\Omega_{\mathrm{VIS}},\Omega_2,\Omega_2-\Omega_1)\Big\}\\ &\times E_{\mathrm{THz}}(\Omega_1)E_{\mathrm{IR}}(\Omega_2-\Omega_1)E^{0}_{\mathrm{VIS}}E_{\mathrm{LO}}(-\Omega_2-\Omega_{\mathrm{VIS}})e^{i(\Omega_2+\Omega_{\mathrm{VIS}})\Delta}.\end{aligned} \tag{12}$$

Similarly, by substituting Eq. (8) into Eq. (10), we obtain for $-\Omega_2$

$$\begin{aligned}\Gamma''(\Omega_2+\Omega_{\mathrm{VIS}},\Omega_1) \propto{}& \Big\{S^{(3)}(-\Omega_2-\Omega_{\mathrm{VIS}},-\Omega_2,\Omega_1)+S^{(3)}(-\Omega_2-\Omega_{\mathrm{VIS}},-\Omega_2,-\Omega_2-\Omega_1)\Big\}\\ &\times E_{\mathrm{THz}}(\Omega_1)E_{\mathrm{IR}}(-\Omega_2-\Omega_1)E^{0}_{\mathrm{VIS}}{}^{*}E_{\mathrm{LO}}(\Omega_2+\Omega_{\mathrm{VIS}})e^{-i(\Omega_2+\Omega_{\mathrm{VIS}})\Delta}.\end{aligned} \tag{13}$$

Equations (12) and (13) show that after the inverse Fourier transformation, the two parts $S_+^{(3)}$ and $S_-^{(3)}$ of the spectrum of the response function are separated in the corresponding spectra Γ' and Γ''.

The considerations above can be boiled down into the following quadrant separation (QS) procedure to separate the two parts of the response function:

1. Create a time delay for the LO pulse relative to the signal pulse.
2. Measure the 2D TIRV data in the time domain by varying the time delay between the THz pulse and the IR/VIS pulse pair. For each time delay, heterodyned, frequency-resolved detection is employed.
3. Perform the Fourier transformation for the acquired time-domain data to obtain the frequency domain spectrum $\Gamma(\Omega_2 + \Omega_{\mathrm{VIS}}, \Omega_1)$.
4. For the spectrum $\Gamma(\Omega_2 + \Omega_{\mathrm{VIS}}, \Omega_1)$, perform Fourier transformation over the frequency axis $\Omega_2 + \Omega_{\mathrm{VIS}}$ to obtain the hybrid time-frequency domain functions $A'(x - \Delta, \Omega_1)$ and $A''(x + \Delta, \Omega_1)$.
5. Perform inverse Fourier transformation separately for the functions $A'(x - \Delta, \Omega_1)$ and $A''(x + \Delta, \Omega_1)$ by applying proper window functions. The transformation generates the spectra $\Gamma'(\Omega_2 + \Omega_{\mathrm{VIS}}, \Omega_1)$ and $\Gamma''(\Omega_2 + \Omega_{\mathrm{VIS}}, \Omega_1)$.

After implementing the QS procedure, we can plot the new spectrum $\tilde{\Gamma}$ as a function of the variables ω_1 and ω_2, which can be positive and negative,

$$\tilde{\Gamma}(\omega_2, \omega_1) = \begin{cases} \Gamma'(\omega_2 + \Omega_{\mathrm{VIS}}, \omega_1), \omega_1 > 0, & \omega_2 > 0(\text{quadrant I}), \\ \Gamma'(\omega_2 + \Omega_{\mathrm{VIS}}, \omega_1), \omega_1 < 0, & \omega_2 > 0(\text{quadrant II}), \\ \Gamma''(-\omega_2 + \Omega_{\mathrm{VIS}}, \omega_1), \omega_1 < 0, & \omega_2 < 0(\text{quadrant III}), \\ \Gamma''(-\omega_2 + \Omega_{\mathrm{VIS}}, \omega_1), \omega_1 > 0, & \omega_2 < 0(\text{quadrant IV}). \end{cases} \quad (14)$$

The new spectrum $\tilde{\Gamma}$ is composed of four quadrants, each of which represents the corresponding quadrant of the response function $S^{(3)}$ (multiplied by the spectra of the THz, IR, and LO pulses). Only two of these four quadrants contain different information, and quadrants I (II) and III (IV) contain complex conjugate data.

To explain the nature of the signal in the different quadrants of the 2D TIRV spectrum, we consider Eqs. (12)–(14) in more detail. We seek to determine how signal frequency relates to frequencies of the THz and IR fields. This relationship is given by the variable frequency Ω_2 in Eqs. (12) and (13). In the previous section, frequency Ω_2 is defined as the difference between the signal frequency and frequency Ω_{VIS} of the VIS pulse (see also the supplementary material and Refs. 6 and 23), and from this definition, consequently, $\Omega_2 > 0$. We consider the signal in the four quadrants separately:

- **Quadrant I**. The signal is given by Eq. (12), with $\Omega_1 > 0$. We denote the frequencies of the THz and IR fields by $\Omega_{\mathrm{THz}}(= |\Omega_1|)$ and $\Omega_{\mathrm{IR}}(= |\Omega_2 - \Omega_1|)$, respectively. Using this notation, we can write $\Omega_2 = \Omega_{\mathrm{THz}} + \Omega_{\mathrm{IR}}$. Thus, the signal in the first quadrant is emitted at the sum frequency of the IR and THz fields.
- **Quadrant II**. The signal is given by Eq. (12), with $\Omega_1 < 0$. We obtain $\Omega_2 = \Omega_{\mathrm{IR}} - \Omega_{\mathrm{THz}}$, because for this quadrant, $\Omega_1 = -\Omega_{\mathrm{THz}}$. Thus, the signal in the second quadrant is emitted at the difference frequency of the IR and THz fields.
- **Quadrant III**. The signal is given by Eq. (13), with $\Omega_1 < 0$. For this quadrant, $\Omega_1 = -\Omega_{\mathrm{THz}}$ and $\Omega_{\mathrm{IR}} = |-\Omega_2 - \Omega_1| = \Omega_2 + \Omega_1$, and we obtain $\Omega_2 = \Omega_{\mathrm{IR}} + \Omega_{\mathrm{THz}}$. Similar to the first quadrant, the signal in the third quadrant is emitted at the sum frequency of the IR and THz fields.
- **Quadrant IV**. The signal is given by Eq. (13), with $\Omega_1 > 0$. For this quadrant, $\Omega_1 = \Omega_{\mathrm{THz}}$, and, similar to the third quadrant, $\Omega_{\mathrm{IR}} = |-\Omega_2 - \Omega_1| = \Omega_2 + \Omega_1$. Thus, $\Omega_2 = \Omega_{\mathrm{IR}} - \Omega_{\mathrm{THz}}$, and the signal is emitted at the difference frequency of the IR and THz fields, which is similar to the second quadrant.

In summary, the signal in quadrants I and III (II and IV) is generated via sum frequency (difference frequency) mixing of the THz and IR fields.

EXPERIMENTAL IMPLEMENTATION

To implement the QS procedure, we modify the experimental setup described in our previous work.[6] The procedure requires an increased time delay between the 2D TIRV signal and LO pulses at the detector. This time delay needs to be stable during the measurements with fluctuations ≪1 fs. To generate and delay an LO with such a high time delay stability, we use a displaced Sagnac interferometer.

A layout of the experimental setup is shown in Fig. 5. The output of an amplified ultrafast Ti:sapphire laser (1 kHz repetition rate, about 60 nm FWHM) is split by the beam splitters BS1 and BS2 into beam 1 (1.0 mJ/pulse), beam 2 (0.8 mJ/pulse), and beam 3 (1.1 mJ/pulse). Beam 1 pumps a commercial traveling-wave optical parametric amplifier of superfluorescence (TOPAS) equipped with a non-collinear difference frequency generation (NDFG) unit. The output of the NDFG unit is a mid-infrared pulse (IR) with a few microjoules of energy, tunable central frequency, and a typical full width at half maximum of about 300 cm^{-1}. The IR pulse is polarized horizontally using the half-wave plate WP and the polarizer P1 and then aligned to the beam combiner (BC), where it is

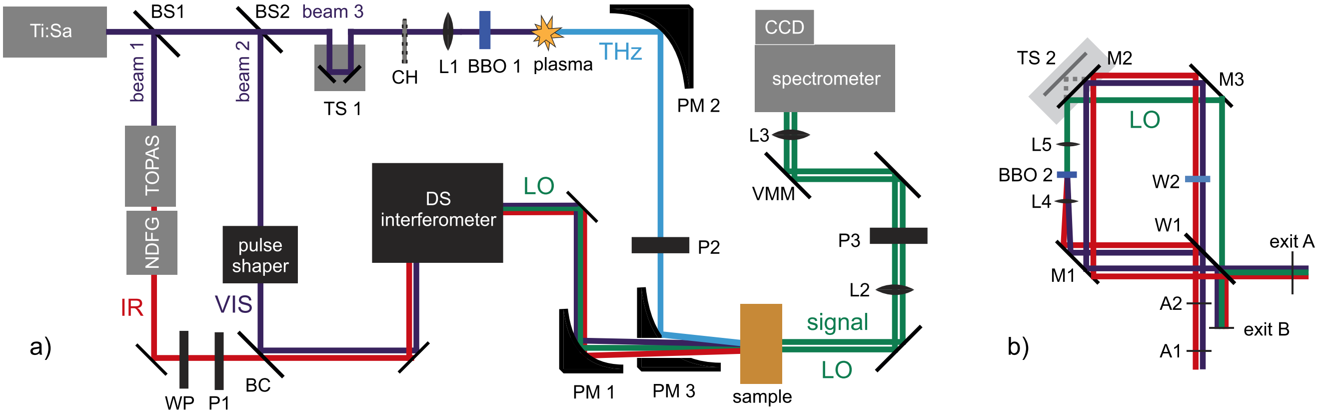

FIG. 5. Schematic of (a) the experimental setup for 2D TIRV spectroscopy and (b) the displaced Sagnac interferometer [labeled the DS interferometer in panel (a)].

overlapped with the horizontally polarized narrowband VIS pulse (about 1 nm FWHM). The VIS pulse is generated from beam 2 using a 4*f* pulse shaper with an optical slit as a mask.[33] After the beam combiner BC, the IR/VIS pulse pair is aligned to the displaced Sagnac interferometer (DS interferometer) to generate the LO pulse.

The DS interferometer [Fig. 5(b)] is composed of a CaF_2 wedge-shaped window W1 and three silver mirrors M1, M2, and M3. Each of these optical elements has a diameter of 2 in., and the wedge of the CaF_2 window is 1°. The IR/VIS pulse pair passes through the window W1, with a small fraction reflected from both the front and the back surfaces. We block the reflection from the front surface and align the reflection from the back surface to pass the clockwise pathway in the interferometer. In the clockwise pathway, the lens L4 (CaF_2, $d = 1/2$ in., $f = 5$ cm) focuses the IR/VIS light at the crystal BBO 2 (a 10 μm thick type 1 BBO crystal on a 2 mm UVFS substrate, Newlight Photonics Inc.). The light produced by sum-frequency generation of the IR and VIS fields in the crystal is collimated by the lens L5 [NBK7, $d = 1/2$ in., $f = 5$ cm, antireflective (AR) coating]. The collimated beam follows the clockwise pathway, and a fraction of it is reflected from the window W1. This reflected light is the LO for the 2D TIRV measurements. At the exit A of the interferometer, the LO is combined with the main fraction of the IR/VIS light, which travels in the counterclockwise pathway. All three beams, the LO and IR/VIS pulses, are focused by the parabolic mirror PM1 ($d = 1.5$ in., $f = 8$ in., bare gold) and overlapped with the THz pulse at the sample.

The THz pulse is generated from beam 3. To this end, beam 3 is focused in a nitrogen atmosphere by lens L1 (NBK7, $f = 20$ cm). Before focusing, beam 3 passes through a 100 μm thick type I BBO crystal (BBO 1) to generate its second harmonic. The focused light ionizes the nitrogen gas, and the non-linear mixing of beam 3 and its second harmonic in the plasma generates a broadband THz pulse.[34,35] The THz spectrum is shown in Fig. S1 of the supplementary material. The emitted THz pulse is collimated by the parabolic mirror PM2, polarized horizontally by the polarizer P2 and focused by the parabolic mirror PM3 at the sample (PM2 and PM3 are 90° off-axis parabolic mirrors with a protected silver coating).

The THz, IR, and VIS pulses interact with the sample, and four-wave mixing of these three fields generates the signal field. The signal propagates together with the LO, which passes through the sample. Lens L2 ($f = 25$ cm) collimates the signal and LO field, and both beams are focused on the entrance slit of the spectrometer (Acton SP2300) by lens L3 ($d = 2$ in. and $f = 10$ cm). After passing the spectrometer, they are detected using a CCD camera (Andor Newton 971 EMCCD). We use polarizer P3 to select the horizontal polarization of the signal field.

To enhance the sensitivity of the experiment, we measure the signal differentially. To this end, we use a chopper CH to modulate the THz beam at the rate of 500 Hz and a vibrating motorized mirror (galvanometer) VMM to separate the LO and LO plus signal fields into two rows 1 and 2 at the chip of the CCD camera. The measured intensity in those two rows is given by

$$I_1 = E_{\mathrm{LO}}^2 \tag{15}$$

and

$$I_2 = E_{\mathrm{LO}}^2 + 2Re\left(E_{\mathrm{LO}}^* E_{\mathrm{sig}}\right) + E_{\mathrm{sig}}^2, \tag{16}$$

where E_{LO} and E_{sig} are the amplitudes of the electric fields of the LO and signal, respectively. The difference $I_2 - I_1$ of these two signals contains the intensity of the signal field E_{sig}^2 and the interference term between the signal and LO fields $2Re\left(E_{\mathrm{LO}}^* E_{\mathrm{sig}}\right)$. This interference term is equal to the right side of Eq. (2).

To align the DS interferometer, we use an alignment laser and the following procedure. We start with the Sagnac interferometer in its non-displaced configuration and align the alignment beam through the irises A1 and A2 [Fig. 5(b)]. Then, we overlap the clockwise and counterclockwise beam pathways inside the interferometer by observing the alignment beam on a paper card. Next, we displace mirror M2, which is installed on the horizontal translation stage TS 2, to offset the clockwise and counterclockwise beam pathways [as shown in Fig. 5(b)]. Then, we improve the collinearity of the clockwise and counterclockwise pathways by monitoring the interference at exit B of the interferometer. When the two pathways are collinear, we mark the position of the clockwise beam close to mirror M2 and install lens L4. We adjust the position of L4 by monitoring the beam at the mark. Next, we install lens L5 and adjust its position by monitoring the interference between the clockwise and counterclockwise beams at exit B. To adjust the time delay between the clockwise and counterclockwise beams, we install a 4 mm thick CaF_2 window W2 in the counterclockwise pathway.

RESULTS AND DISCUSSION

To validate the approach described in the theoretical section, we use CaF_2 and nitrogen gas as two model samples. Nitrogen gas is often used in terahertz field induced second harmonic (TFISH) generation to measure the time profile of a THz pulse.[36,37] This material represents the case of a non-resonant interaction with all three pulses (THz, IR, and VIS) in the frequency range of the present work. In contrast, CaF_2 represents the case of a resonant interaction with the THz pulse and a non-resonant interaction with the IR and VIS pulses.

2D TIRV spectroscopy of CaF_2

Figure 6(a) shows the time-domain 2D TIRV data measured for a 2 mm thick CaF_2 window (step 2 of the QS procedure) by scanning the time delay between the THz pulse and the IR/VIS pulse pair. The ordinate axis Ω_2 is obtained by subtracting Ω_{VIS} from the signal frequency. By Fourier transformation over the horizontal axis of these time-domain data, we obtain the 2D TIRV spectrum, as shown in Fig. 6(b) (step 3 of the QS procedure). The two peaks in this spectrum at $\Omega_1 = \pm 66\ \mathrm{cm}^{-1}$ correspond to the resonant excitation of the CaF_2 phonon mode by the THz pulse.[6,38] The third peak at $\Omega_1 = 0\ \mathrm{cm}^{-1}$ is generated mainly by the homodyne-detected 2D TIRV signal field (which is the intensity of this electromagnetic wave). The two quadrants I and II shown in Fig. 6(b) contain complex conjugate data: The spectrum in quadrant I is composed of the sum of the two parts of the CaF_2 response function, $S^{(3)}(\Omega_2 + \Omega_{\mathrm{VIS}}, \Omega_2, \Omega_1 > 0)$ and $S^{(3)}(-\Omega_2 - \Omega_{\mathrm{VIS}}, -\Omega_2, \Omega_1 > 0)$ [multiplied by the spectra of the THz, IR, and LO pulses, Eq. (3)]. Similarly, the spectrum in quadrant II is composed of the sum of $S^{(3)}(\Omega_2 + \Omega_{\mathrm{VIS}}, \Omega_2, \Omega_1 < 0)$ and $S^{(3)}(-\Omega_2 - \Omega_{\mathrm{VIS}}, -\Omega_2, \Omega_1 < 0)$. The response along the Ω_2-axis reflects the bandwidth of the infrared laser pulse.

Figure 6(c) shows the hybrid time-frequency data produced by Fourier transformation of the (complex-valued) data shown in Fig. 6(b) over the vertical axis (step 4 of the QS procedure). The peaks α1 and α2, located at $\omega_1 = \mp 66\ \mathrm{cm}^{-1}$ and $x = \pm 4.1$ ps, are produced by the interference between the 2D TIRV signal and the LO. These two peaks correspond to the neat 2D TIRV spectrum of CaF_2. The other five peaks (β, γ1, γ2, δ1, and δ2) are artifacts of the measurement. Peak β, located at $\omega_1 = 0\ \mathrm{cm}^{-1}$ and $x = 0$ ps, stems from the homodyne-detected 2D TIRV signal field. Peaks γ1 and γ2 are located at $\omega_1 = \mp 66\ \mathrm{cm}^{-1}$ and $x = \pm 0.2$ ps, which indicates the existence of a second local oscillator pulse. This local oscillator ghost has a 0.2 ps time delay relative to the 2D TIRV signal pulse. The interference between the signal and the LO ghost pulse produces the peaks γ1 and γ2. The peaks δ1 and δ2 are located at $\omega_1 = 0\ \mathrm{cm}^{-1}$ and $x = \pm 3.9$ ps. The frequency ω_1 of these peaks shows that they are generated by a 2D TIRV signal, which does not oscillate with the time delay between the THz and IR/VIS pulses. The nature of this signal is not yet fully clear to us. However, from the time x of δ1 and δ2, we conclude that they are produced by interference with the LO rather than the LO ghost.

In our setup, we use a collinear geometry, in which the IR and VIS pulses travel together after the BC [Fig. 5(a)]. Therefore, it is likely that the LO ghost is produced by sum-frequency generation of the IR and VIS pulses upon reflection on one or several of the mirrors on their pathway. To verify the assignment of the peaks shown in Fig. 6(c), we perform two additional measurements. In the first measurement, we install an additional CaF_2 plate of ≈0.42 mm thickness into the LO pathway in the DS interferometer. This plate increases the optical path length to the detector for the LO by about 0.6 ps and causes a shift in the peaks α1 and α2 to $x = \pm 4.7$ ps as well as the peaks δ1 and δ2 to $x = \pm 4.5$ ps [Fig. 6(d)]. We note that all other peaks remain at their initial positions. In the second measurement, we block the LO beam in the DS interferometer. This leads to disappearance of all peaks, except peaks β, γ1, and γ2 [Fig. 6(e)]. The results of these two additional measurements confirm the assignment of the peaks: α1 and α2 are the peaks of interest, β is the homodyne signal, and γ- and δ-peaks are ghost signals.

To implement step 5 of the QS procedure using Eqs. (9) and (10), we need to determine the integration limits $\pm a + \Delta$ and $\pm a - \Delta$ for the functions A' and A'', respectively. To this end, we need to determine the sign of the LO time offset Δ. This sign can be found by comparing the data shown in Figs. 6(c) and 6(d). The LO optical path length increases by adding the CaF_2 plate, and simultaneously, the time delay between the LO and signal pulses increases. Thus, the LO arrives at the detector after the signal pulse and $\Delta < 0$. Therefore, the inverse Fourier transformation of the peaks α2 (A') and α1 (A'') generates Γ' and Γ'', respectively. We use a rectangular window function to filter out the peaks β, γ1, γ2, δ1, and δ2 before the inverse Fourier transformation [window function is shown by the yellow rectangles in Fig. 6(c)]. Figure 6(f) shows the obtained 2D TIRV spectrum for CaF_2 after the last Fourier transformation (step 5 of the QS procedure). In this plot, we use the variables $-\infty < \omega_1, \omega_2 < +\infty$ for the frequency axes. The CaF_2 response appears only in the first and third quadrants of the spectrum, which means that only interactions with $\omega_2 = \Omega_{\mathrm{IR}} + \Omega_{\mathrm{THz}}$ contribute to the signal generation. Such generation can be considered using the pathways A and/or B shown in Fig. 2 with a second virtual state instead of the HFM state.

To verify this conclusion, we modulate the spectrum of the IR pulse before it interacts with the sample. We use a thin (~10 μm) polyethylene film to deplete the IR intensity at 2850 and 2920 cm^{-1} by the C—H stretch absorption. Figure 6(g) shows a comparison of the original IR spectrum, the modulated IR spectrum, and the profile of the 2D TIRV spectrum of CaF_2 along the ω_2-axis, which is measured with the modulated IR spectrum. The depletion of the IR spectrum causes two minima in the 2D TIRV spectrum, which are offset by +66 cm^{-1} relative to the frequencies of the C—H vibrations. This offset is exactly the frequency of the phonon resonance excited by the THz pulse. Thus, for CaF_2, the frequency of the signal is indeed given by the sum of the THz and IR (and VIS) frequencies.

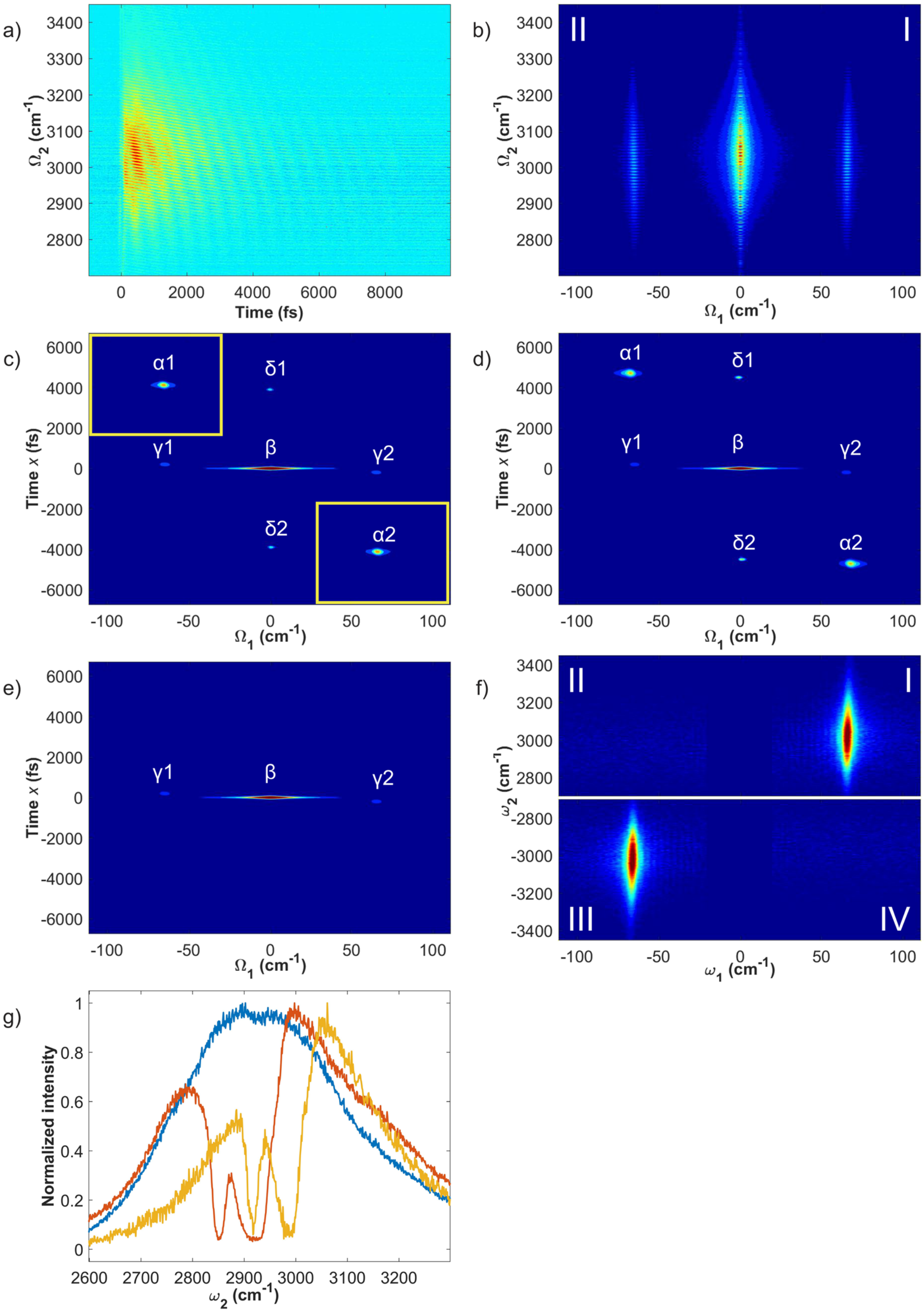

FIG. 6. Measured 2D TIRV spectroscopy data of a CaF_2 sample: (a) the 2D TIRV signal measured for different time delays (horizontal axis) between the THz and IR/VIS pulses (step 2 of the QS procedure), (b) the absolute-value 2D TIRV spectrum obtained by Fourier transformation of the data in (a) (step 3 of the QS procedure), (c) hybrid time-frequency representation of the 2D TIRV data obtained by Fourier transformation of the data in (b) along the vertical axis (step 4 of the QS procedure), (d) and (e) the same as (c) but measured with an additional time delay of the LO and blocked LO, respectively, (f) the absolute-value 2D TIRV spectrum of CaF_2 obtained by inverse Fourier transformation of peaks α1 and α2 in (c), and (g) the profile of the absolute-value 2D TIRV spectrum of CaF_2 along the ω_2 axis measured with a modulated IR pulse (yellow line). Blue and red lines show spectra of the original and modulated IR pulses, respectively.

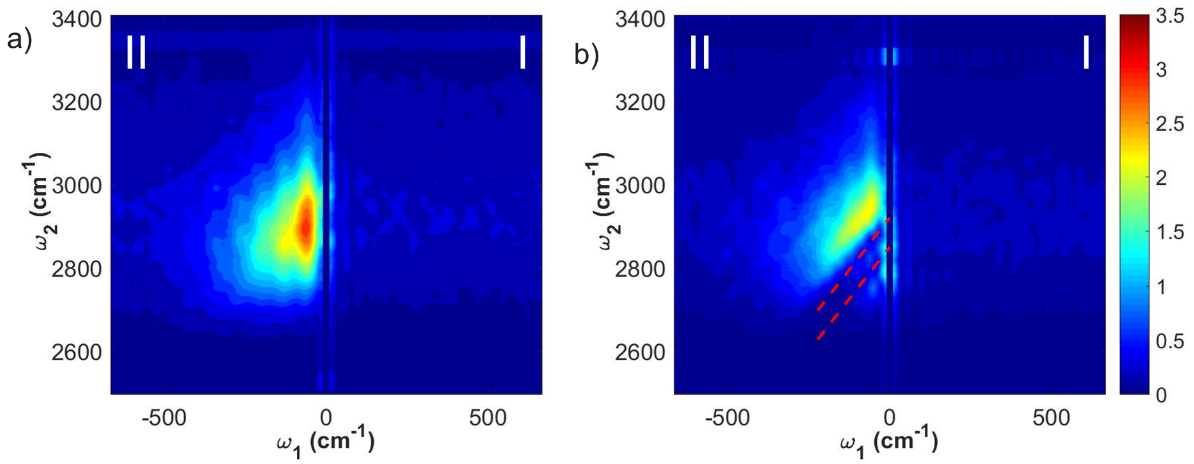

FIG. 7. Absolute-value 2D TIRV spectra of nitrogen gas measured using the (a) original and (b) modulated IR pulse.

2D TIRV spectroscopy of nitrogen gas

Figure 7 shows the 2D TIRV spectrum of nitrogen gas obtained by using the QS procedure. Here, we show the spectrum only for positive ω_2 frequencies (quadrants I and II) since quadrants III and IV contain complex conjugate information. In contrast to CaF_2, the nitrogen signal appears only in the second quadrant. The broad line shape of the peak is consistent with the non-resonant character of the nitrogen response. For the signal to appear in the second quadrant, it should be produced by difference frequency generation between the IR and THz pulses. Indeed, the peak has an apparent slope where the higher THz frequency corresponds to the lower frequency of the signal. To better measure the slope of the peak, we use a depleted IR spectrum, similar to the CaF_2 measurements. The absorption lines in the IR spectrum at 2850 and 2920 cm^{-1} cause a depletion of the 2D TIRV spectrum along the lines $\omega_2 = \omega_1 + 2850$ cm^{-1} and $\omega_2 = \omega_1 + 2920$ cm^{-1} [red dashed lines in Fig. 7(b)].

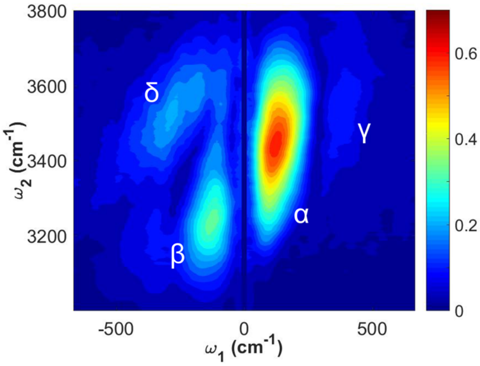

FIG. 8. Absolute-value 2D TIRV spectrum of liquid water with separated quadrants (only positive ω_2-frequencies are shown).

In conclusion, the data for CaF_2 and nitrogen gas validate the ability of the QS procedure to separate different excitation pathways in 2D TIRV spectroscopy. We can now use it for substances with more complex 2D TIRV response, such as liquid water. Liquid water previously demonstrated complications of the 2D TIRV spectrum due to the overlay of signals belonging to different quadrants. In the following, we employ the QS procedure to separate the signals and simplify the spectrum of neat H_2O.

2D TIRV spectroscopy of liquid H_2O

Figure 8 shows the 2D TIRV spectrum of neat liquid water at room temperature. In contrast to CaF_2 and nitrogen, the response of water appears in all quadrants of the spectrum. The peaks α and β dominating the first and second quadrants are located at ($\omega_1 \approx 125$ cm^{-1}, $\omega_2 \approx 3440$ cm^{-1}) and ($\omega_1 \approx -125$ cm^{-1}, $\omega_2 \approx 3240$ cm^{-1}), respectively. Based on previous work,[6] we assign these peaks to the coupling between the intramolecular O—H stretch and intermolecular hydrogen bond stretch and bending modes. The separation of the different excitation pathways into different quadrants eliminates the characteristic minimum of intensity at $\Omega_2 \approx 3250$ cm^{-1} (Fig. 1 and Ref. 6), which is consistent with the interpretation that the minimum originates from the interference of signals of different quadrants. In addition to the peaks α and β, the spectrum contains peaks γ and δ, which have not been observed before. We assign these peaks to the coupling between the O—H stretch and the librational modes of water. A detailed investigation of the 2D TIRV spectrum of water is beyond the scope of the present work and will be provided elsewhere.

CONCLUSIONS

In non-linear spectroscopy that does not excite population states, the interference of different excitation pathways can prohibit a straightforward interpretation of the spectra. This is particularly true for 2D TIRV spectroscopy, where sum and difference frequency mixing between infrared and terahertz fields can lead to complex line shapes. The quadrant separation procedure reported here provides a method to disentangle excitation pathways and analyze them separately. Some materials like CaF_2 and N_2 have one dominating type (sum or difference) of frequency mixing. Even for such simple cases, the method is useful for determining the excitation pathway producing the signal. It is even more beneficial for samples that generate signals via both sum and difference frequency mixing, as illustrated by the case of liquid water. Interestingly, the ratio between sum and difference frequency mixing of infrared and terahertz fields varies dramatically for different samples. 2D TIRV spectra with separated quadrants simplify interpretation and analysis of the LFM–HFM coupling, which can be interesting for a variety of soft matter systems.

SUPPLEMENTARY MATERIAL

See the supplementary material for the theoretical formalism of 2D TIRV spectroscopy and the spectrum of the THz pulse.

ACKNOWLEDGMENTS

This work was financially supported by the MaxWater Initiative from the Max Planck Society.

DATA AVAILABILITY

The data that support the findings of this study are available from the corresponding author upon reasonable request.

REFERENCES

[1] P. Hamm and M. T. Zanni, *Concepts and Methods of 2D Infrared Spectroscopy* (Cambridge University Press, Cambridge, 2011).

[2] S. Mukamel, A. Piryatinski, and V. Chernyak, Acc. Chem. Res. **32**, 145 (1999).

[3] M. Khalil, N. Demirdöven, and A. Tokmakoff, J. Phys. Chem. A **107**, 5258 (2003).

[4] T. L. C. Jansen, B. M. Auer, M. Yang, and J. L. Skinner, J. Chem. Phys. **132**, 224503 (2010).

[5] S. T. Roberts, R. A. Nicodemus, A. Mandal, and A. Tokmakoff, J. Chem. Phys. **135**, 054509 (2011).

[6] M. Grechko, T. Hasegawa, F. D'Angelo, H. Ito, D. Turchinovich, Y. Nagata, and M. Bonn, Nat. Commun. **9**, 885 (2018).

[7] M. Grechko, S. A. Bretschneider, L. Vietze, H. Kim, and M. Bonn, Angew. Chem., Int. Ed. **57**, 13657 (2018).

[8] M. Khalil, N. Demirdöven, and A. Tokmakoff, Phys. Rev. Lett. **90**(4), 047401 (2003).

[9] J. D. Hybl, A. Albrecht Ferro, and D. M. Jonas, J. Chem. Phys. **115**, 6606 (2001).

[10] M. Woerner, W. Kuehn, P. Bowlan, K. Reimann, and T. Elsaesser, New J. Phys. **15**, 025039 (2013).

[11] P. Hamm and A. Shalit, J. Chem. Phys. **146**, 130901 (2017).

[12] P. Hamm and J. Savolainen, J. Chem. Phys. **136**, 094516 (2012).

[13] J. Savolainen, S. Ahmed, and P. Hamm, Proc. Natl. Acad. Sci. U. S. A. **110**, 20402 (2013).

[14] G. Mead, H.-W. Lin, I.-B. Magdău, T. F. Miller, and G. A. Blake, J. Phys. Chem. B **124**, 8904 (2020).

[15] I. A. Finneran, R. Welsch, M. A. Allodi, T. F. Miller, and G. A. Blake, Proc. Natl. Acad. Sci. U. S. A. **113**, 6857 (2016).

[16] I. A. Finneran, R. Welsch, M. A. Allodi, T. F. Miller, and G. A. Blake, J. Phys. Chem. Lett. **8**, 4640 (2017).

[17] P. M. Donaldson, Chem. Sci. **11**, 8862 (2020).

[18] W. Zhao and J. C. Wright, Phys. Rev. Lett. **84**, 1411 (2000).

[19] P. M. Donaldson, R. Guo, F. Fournier, E. M. Gardner, I. R. Gould, and D. R. Klug, Chem. Phys. **350**, 201 (2008).

[20] E. S. Boyle, A. V. Pakoulev, and J. C. Wright, J. Phys. Chem. A **117**, 5578 (2013).

[21] M. Cho, Phys. Rev. A **61**, 023406 (2000).

[22] M. Cho, J. Chem. Phys. **111**, 4140 (1999).

[23] L. Vietze, M. Bonn, and M. Grechko, *Coherent Multidimensional Spectroscopy*, Springer Series in Optical Sciences (Springer, Singapore, 2019), pp. 197–214.

[24] M. Cho, J. Chem. Phys. **111**, 10587 (1999).

[25] S. Yamaguchi and T. Tahara, J. Chem. Phys. **129**, 101102 (2008).

[26] S. Nihonyanagi, S. Yamaguchi, and T. Tahara, J. Chem. Phys. **130**, 204704 (2009).

[27] S. Mukamel, *Principles of Nonlinear Optical Spectroscopy* (Oxford University Press, Oxford, 1995).

[28] *Advances in Infrared and Raman Spectroscopy*, edited by R. J. H. Clark and R. E. Hester (Wiley, 1985).

[29] C. C. Rich, M. A. Mattson, and A. T. Krummel, J. Phys. Chem. C **120**, 6601 (2016).

[30] H. Vanselous and P. B. Petersen, J. Phys. Chem. C **120**, 8175 (2016).

[31] R. E. Pool, J. Versluis, E. H. G. Backus, and M. Bonn, J. Phys. Chem. B **115**, 15362 (2011).

[32] M. Thämer, R. K. Campen, and M. Wolf, Phys. Chem. Chem. Phys. **20**, 25875 (2018).

[33] A. M. Weiner, J. P. Heritage, and E. M. Kirschner, J. Opt. Soc. Am. B **5**, 1563 (1988).

[34] J. Dai, J. Liu, and X.-C. Zhang, IEEE J. Sel. Top. Quantum Electron. **17**, 183 (2011).

[35] H. G. Roskos, M. D. Thomson, M. Kreß, and T. Löffler, Laser Photonics Rev. **1**, 349 (2007).

[36] X. Lu, N. Karpowicz, Y. Chen, and X.-C. Zhang, Appl. Phys. Lett. **93**, 261106 (2008).

[37] J. Dai, X. Xie, and X. C. Zhang, Phys. Rev. Lett. **97**, 103903 (2006).

[38] Y. Wang, L. A. Zhang, S. Shang, Z.-K. Liu, and L.-Q. Chen, Phys. Rev. B **88**, 024304 (2013).